

Phonon-Induced Transparency in Functionalized Single Layer Graphene

Bruno Rousseau,¹ François Lapointe,² Minh Nguyen,² Maxime Biron,³ Etienne Gaufrès,² Saman Choubak,³ Zheng Han,^{4,5} Vincent Bouchiat,^{4,5} Patrick Desjardins,³ Michel Côté,^{1,*} and Richard Martel^{2,†}

¹*Regroupement Québécois sur les Matériaux de Pointe and Département de physique, Université de Montréal, C. P. 6128, Succursale Centre-Ville, Montréal, Québec H3C 3J7, Canada*

²*Regroupement Québécois sur les Matériaux de Pointe and Département de chimie, Université de Montréal, C. P. 6128, Succursale Centre-Ville, Montréal, Québec H3C 3J7, Canada*

³*Regroupement Québécois sur les Matériaux de Pointe and Département de génie physique, École Polytechnique de Montréal, C. P. 6079, Succursale Centre-ville, Montréal, Québec H3C 3A7, Canada*

⁴*Université de Grenoble, Alpes, Institut NÉEL, F-38042 Grenoble, France*

⁵*CNRS, Institut NÉEL, F-38042 Grenoble, France*

Herein, intervalley scattering is exploited to account for anomalous antiresonances in the infrared spectra of doped and disordered single layer graphene. We present infrared spectroscopy measurements of graphene grafted with iodophenyl moieties in both reflection microscopy and transmission configurations. Asymmetric transparency windows at energies corresponding to phonon modes near the Γ and K points are observed, in contrast to the featureless spectrum of pristine graphene. These asymmetric antiresonances are demonstrated to vary as a function of the chemical potential. We propose a model which involves coherent intraband scattering with defects and phonons, thus relaxing the optical selection rule forbidding access to $\mathbf{q} \neq \Gamma$ phonons. This interpretation of the new phenomenon is supported by our numerical simulations that reproduce the experimental features.

Graphene has found promising applications in plasmonics for the terahertz (THz) to mid-infrared (MIR) regime because of the optical properties pertaining to its bidimensional semimetallic nature [1]. In this energy range, its absorption spectrum is dominated by a strong Drude-like response that can be modulated by doping [2]. The optical response is, however, monotonous because there is no infrared-active phonon mode available, a fact explained by Zallen's rule stating that at least three atoms in the primitive unit cell are necessary (and sufficient) to generate infrared activity in an elemental crystal [3]. Tailoring the optical response of single layer graphene (SLG) has therefore required creating plasmonic resonators and metamaterials by patterning the material into nanoribbons [4–6], nanodisks, heterostructure stacks [7], etc. In contrast, pristine bilayer graphene (BLG) demonstrates a native tunable Fano resonance [8, 9], while BLG nanoribbons exhibit phonon-induced transparency through plasmon-phonon coupling [10].

We report on a novel scattering phenomenon mediated by phonons and disorder, and its manifestation in the MIR spectra of single layer graphene (SLG). The infrared spectra of covalently functionalized graphene show Fano-like antiresonances which we demonstrate to emerge from scattering with randomly distributed grafts, thereby allowing momentum transfer between phonons and electronic intraband excitations. The scattering process leads to sharp transparency windows in the mid-infrared optical conductivity at frequencies corresponding to optical phonon energies for momenta near the Γ and $\pm K$ points, the latter being a direct consequence of intervalley scattering. The mechanism is reminiscent, but distinct, of the double resonance scattering process

between the two Dirac cones of graphene, that leads to the occurrence of the D band in Raman spectroscopy of disordered samples [11]. The phenomenon appears ubiquitous to low dimension carbon structures such as carbon nanotubes [12], and can potentially be exploited in optoelectronic applications in the infrared.

RESULTS

Pristine and disordered SLG samples

Our samples consist of single layer graphene grown on copper foil using a specific intermittent growth chemical vapor deposition (CVD) process that allows production of a fully homogeneous monolayer without multilayer patches [13]. The graphene thus obtained was then transferred to a MIR transparent substrate with regular transfer techniques [14]. The graphene sheets have been fully characterized through optical and scanning electron microscopy, along with Raman microspectroscopy and hyperspectral cartography to ensure that there is no bilayer contamination within the investigated regions (see Supplementary Information). Covalent functionalization is then used to introduce disorder in the crystalline lattice [15–17]. Indeed, grafting of iodophenyl moieties (I-Ph) to graphene breaks the sp^2 conjugation and generates sp^3 hybridized scattering centers [18]. The reaction, however, leaves the samples in a state where the Fermi level is poorly defined from adsorbed ions and grafts. We thus use chemical doping to set the chemical potential. Practically, this is achieved by soaking the sample in a doping solution at a certain concentration, and then drying in a stream of nitrogen, which leaves the adsorbed dopant

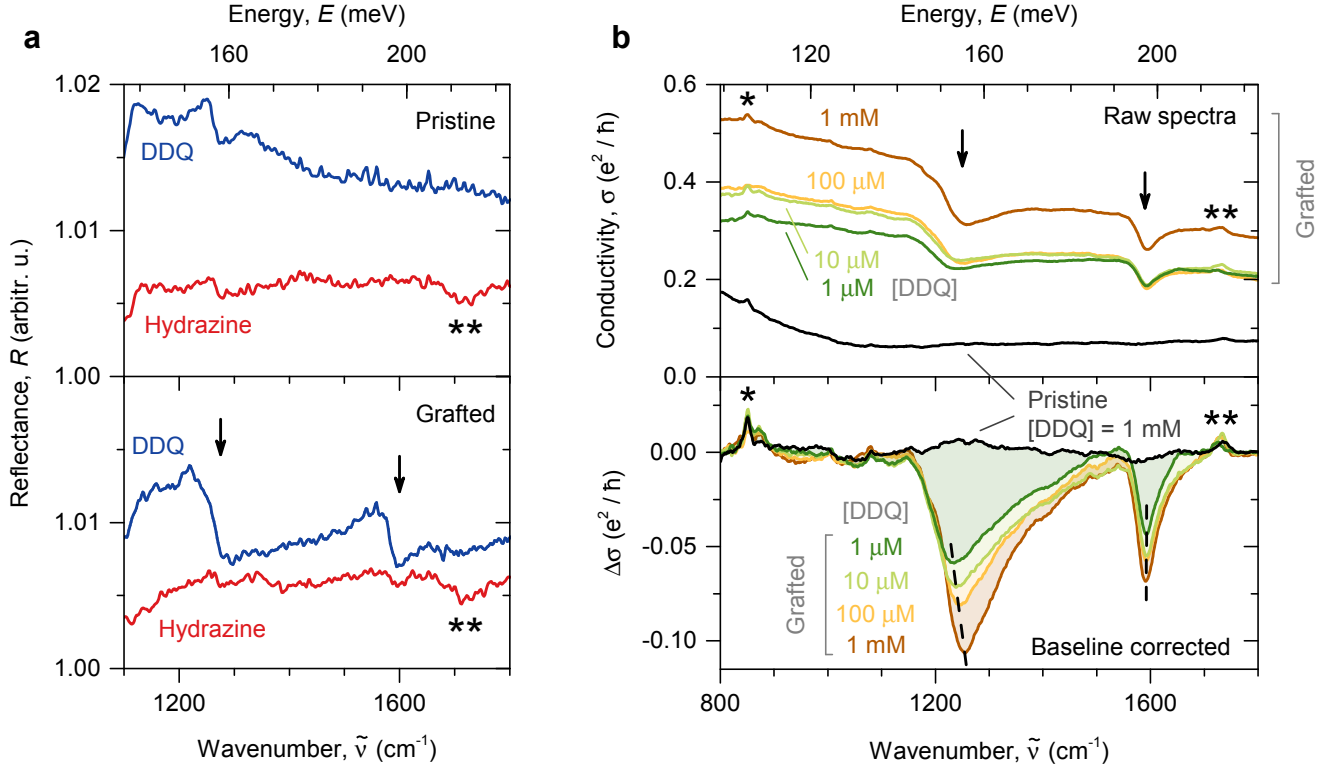


FIG. 1. (a) Mid-infrared reflection spectra in microscopy of pristine (upper panel) and electrografted single layer graphene (lower panel) transferred onto intrinsic silicon with 300 nm thermal oxide. Spectra are shown after soaking in dopant solutions of $[\text{DDQ}] = 1 \text{ mM}$ and $[\text{hydrazine}] = 10 \text{ mM}$ in acetonitrile. (b) Mid-infrared optical conductivity of single layer graphene on BaF_2 measured in transmission. Raw spectra are presented in the upper panel, while the lower panel shows traces after subtraction of a cubic baseline. The black trace comes from a pristine sample doped at $[\text{DDQ}] = 1 \text{ mM}$. The other traces belong to a functionalized sample for varying DDQ concentrations. The arrows show the disorder-induced antiresonances, while the star (*) denotes a spurious band, and the double stars (**), the carbonyl band of an impurity.

molecules on the surface. For instance, 2,3-dichloro-5,6-dicyano-1,4-benzoquinone (DDQ, an electron acceptor) dissolved in acetonitrile is used for *p*-type doping, while hydrazine (an electron donor) in acetonitrile allows reduction of graphene.

Phonon-induced transparencies in MIR response

Infrared spectroscopy measurements are presented in Fig. 1. The first set of data presented in (a) shows the results of microscopy measurements in reflection mode of SLG transferred onto intrinsic silicon with 300 nm thermal oxide, which allowed us to probe well characterized regions of the sample and to exclude areas with bilayer and few-layer islands. Except for a weak modulation near 1250 cm^{-1} and the carbonyl band of an impurity at $\sim 1720 \text{ cm}^{-1}$ (denoted by **), pristine graphene yields a featureless MIR spectrum in both doping states (*i.e.* $[\text{DDQ}] = 1 \text{ mM}$ and $[\text{hydrazine}] = 10 \text{ mM}$) [Fig. 1(a), top panel]. This behavior is expected since no graphene phonons are supposed to be infrared-active [19]. In accordance with our following arguments, the weak modu-

lation near 1250 cm^{-1} may be due to the fact that the probed area contains wrinkles and joint boundaries between crystal domains (see microscopy pictures in Supplementary Information), which are sources of disorder. The observations, however, change drastically upon covalent grafting to graphene [graft density of approximately 1 I-Ph for 100 C atoms as evaluated by iodine content analysis by X-ray photoelectron spectroscopy (XPS), see Supplementary Information]. As seen in the bottom panel of Fig. 1(a), a broad asymmetric signal is now apparent near 1600 cm^{-1} in the DDQ-doped trace, and a second, even broader signal is also observed around 1250 cm^{-1} . Vibrational bands from dopants and I-Ph are absent from the spectra because their concentrations are lower than the detection limit. Moreover, the asymmetric bands disappear upon soaking in a hydrazine solution, and can be recovered by doping back to *p*-type (see Supplementary Information), thus demonstrating a dependency on charge carrier density.

The optical window of SiO_2 being limited in the infrared by an intense absorption band at $\sim 1050 \text{ cm}^{-1}$, transmission spectra were obtained on a BaF_2 substrate to better assess the graphene band observed at

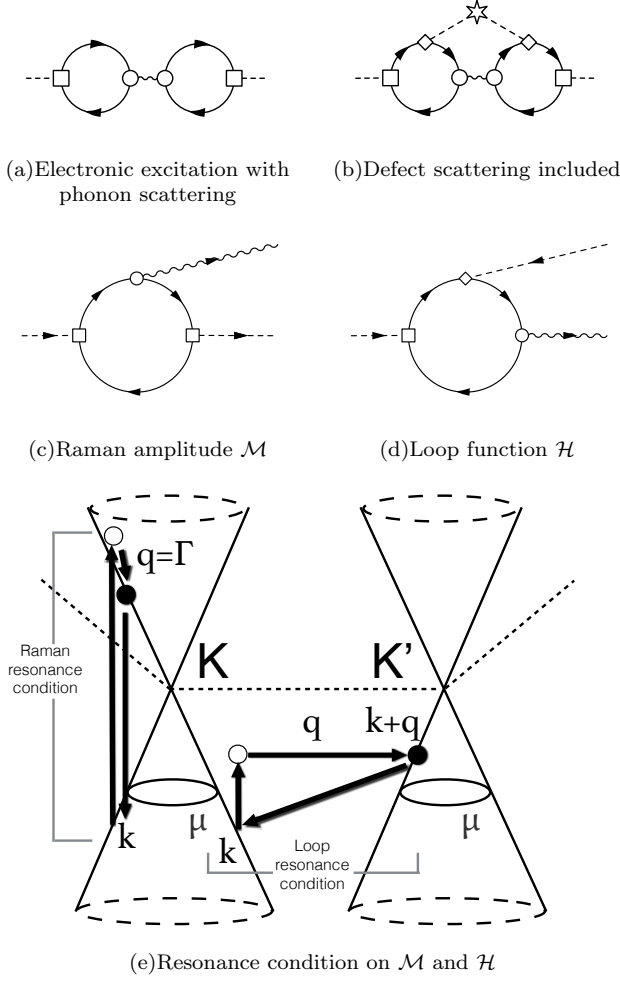


FIG. 2. (a-b-c-d) Various Feynman diagrams. The squares represent the matrix elements of the light-electron interaction, the circles represent the electron-phonon coupling, the diamonds the self-consistent, energy dependent defect scattering potential, the star corresponds to a factor of n_{imp} (the number density of defects), the full lines the electronic Green functions and the wavy lines the phonon propagator. (a) Contribution to the current-current correlation function, which leads to a Fano profile in bilayer graphene but vanishes identically in single layer graphene, (b) extension involving both phonon and defect scattering beyond electronic self-energy effects, thus leading to optical bands that are forbidden in pristine samples. (c) Feynman diagram corresponding to a Raman scattering resonance. (d) Feynman diagram corresponding to the loop function. (e) Schematics of the resonant scattering mechanisms for both Raman spectroscopy and the loop function.

$\sim 1250 \text{ cm}^{-1}$. In these measurements, macroscopic sample areas were probed to prove that the effect is not limited to localized microscopic regions. This second set of data is shown in Fig. 1(b) using an optical conductivity scale for pristine graphene doped at $[\text{DDQ}] = 1 \text{ mM}$, and for grafted graphene (graft density of approximately 2 I-Ph for 100 C atoms as evaluated by XPS) p -doped at

various levels (from $[\text{DDQ}] = 1 \mu\text{M}$ to 1 mM). Raw spectra are presented in the top panel, while a cubic baseline has been subtracted from all spectra in the lower panel. Two antiresonances are identified at $\sim 1250 \text{ cm}^{-1}$ and $\sim 1600 \text{ cm}^{-1}$, whereas the pristine signal (black trace) is smooth, to the exception of a spurious band denoted by a star (*), and the carbonyl band of an impurity marked by double stars (**). The frequencies of the antiresonances coincide with those of the Raman D and G bands, thus strongly suggesting that phonon modes are involved in the mechanism. The profiles of the antiresonances are asymmetric and skewed toward higher energies. The widths of the bands, as evaluated by fitting a Fano profile, are approximatively 120 cm^{-1} and 45 cm^{-1} respectively for the lower and higher energy bands. Moreover, the amplitude of these anomalies can be modulated with dopant concentration, which becomes evident after baseline correction (bottom panel). As can be observed in the top panel, the background absorption also evolves following the known dependence of the Drude peak to doping [2], thus supporting the fact that the signal cross section is related to charge carrier density. It should be stressed that the observed transparency windows (antiresonances) are important hints about the underlying mechanism, since it is in discrepancy with normal phonon resonances which absorb light and thus would yield upward bands on a conductivity scale.

Extension to the Drude model

To first gain intuition about the physics underpinning the occurrence of the antiresonances, we begin by extending the Drude model to collisions between a representative semiclassical electron and a phonon mode. Requiring only momentum and energy conservation, we derive the following expression for the conductivity σ (Sec. III-A, Supplementary Information):

$$\text{Re}[\sigma(\omega)] \simeq \sigma_0 \frac{(2\Gamma)^2}{(2\Gamma)^2 + (\hbar\omega)^2} + \Delta\sigma(\omega) \quad (1)$$

$$\frac{\Delta\sigma(\omega)}{\sigma_0} \propto \frac{m}{M} \text{Im} \left[\frac{(2\Gamma)^3}{(\hbar\omega + 2i\Gamma)^2} \mathcal{D}_{ph}(\omega) \right], \quad (2)$$

where σ_0 is the static Drude conductivity, m/M is the ratio of electronic to ionic mass, 2Γ is the width of the Drude peak and $\mathcal{D}_{ph}(\omega)$ is the Green function of the phonon mode which is sharply peaked at the frequency of the phonon. The first term in Eq. (1) is the familiar Drude conductivity, while the second term accounts for an interference effect induced by multiple subsequent electron-phonon scattering events and the dynamical nature of the phonon. For $\hbar\omega > 2\Gamma$, this simple model reproduces asymmetric antiresonances skewed toward higher energies and centered at the phonon frequency (Fig. S10, Supplementary Information).

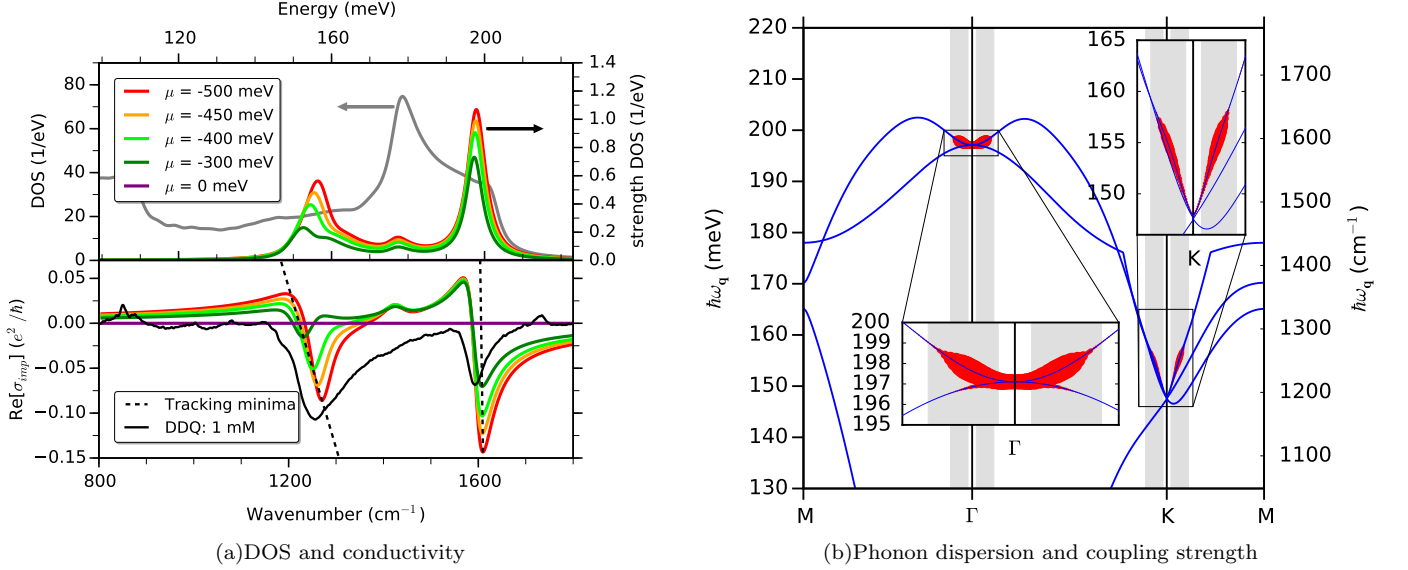


FIG. 3. (a) Computed phonon density of states and density of states weighted with the phonon coupling strength $P_{\nu\mathbf{q}}$ (top panel); computed contributions to the conductivity for various chemical potential values, compared to experimental results corresponding to [DDQ] = 1 mM (lower panel). (b) Model phonon dispersion of graphene (thin blue lines) overlaid with the phonon coupling strength (thick red regions): the region size is proportional to the corresponding $P_{\nu\mathbf{q}}$ value. The vertical grey bands indicate sections of the first Brillouin zone where the resonance conditions are satisfied for $\hbar\omega = 200$ meV with the chemical potential μ set to -450 meV and the energy zero corresponds to the Dirac point.

Quantum mechanics model

While this simple extension to the Drude model gives an intuitive picture for the underlying physics at play, it is not sufficiently sophisticated as it does not account for the quantum mechanical nature of electrons and phonons, nor does it take into consideration selection rules or band dispersion. A proper treatment of the optical conductivity makes use of the Kubo formula [20], which relates $\sigma(\omega)$ to the current-current correlation function. The effects of electron-phonon coupling as well as defect scattering can then be computed systematically using the machinery of perturbation theory and Feynman diagrams, an approach which treats both *intraband* and *interband* electronic excitations on equal footing. The fully quantum mechanical mechanism corresponding to the simple model of Eq. (1) is described by the Feynman diagram of Fig. 2(a) in the case where *intraband* electronic excitations (*ie*, excitations near the Fermi energy) dominate. This same Feynman diagram, but with an emphasis on *interband* electronic excitations, was first proposed by Cappelluti *et al.* [21, 22] to explain the Fano profile observed in pristine bilayer graphene [8, 9] and few-layer graphene [23], where a discrete mode (a tangential phonon mode at Γ) couples to the continuum of electron-hole excitations responsible for an optical resonance. This mechanism was also applied to plasmon-phonon coupling to account for similar observations in

bilayer graphene nanoribbons [10]. In pristine single layer graphene, however, a Fano resonance has never been observed, nor is it expected: indeed, the contribution from the mechanism of Fig. 2(a) vanishes by symmetry. Even more, the other observed band at $\sim 1250 \text{ cm}^{-1}$ cannot be attributed to coupling to Γ point phonons, as there are no available phonon modes near this energy.

A key point to correctly model the observed phenomenon is the introduction of lattice defects (I-Ph grafting), which destroys the periodicity of the system. Its simplest consequence is a reduction of the electronic lifetime, leading to a broader Drude peak. However, the introduction of electronic damping in the mechanism of Fig. 2(a) still leads to an expression which vanishes by symmetry in single layer graphene; the effect of disorder must thus be treated beyond electronic lifetime reduction. Averaging the current-current correlation function over all possible graft configurations, the simplest disorder contribution coupling non- Γ phonons to electronic excitations is given by the Feynman diagram of Fig. 2(b). It is shown in the Supplementary Information to yield a contribution to the conductivity of the form

$$\text{Re}[\sigma_{\text{imp}}(\omega)] \simeq \frac{e^2}{\hbar} (n_{\text{imp}} a_0^2) \sum_{\alpha=x,y} \sum_{L=A,B} \frac{1}{N} \sum_{\nu\mathbf{q}} A_{\nu\mathbf{q}}^{\alpha L} \frac{|Q_{\nu\mathbf{q}}^{\alpha L}|^2 - 1 + 2z_{\nu\mathbf{q}} \text{Re}[Q_{\nu\mathbf{q}}^{\alpha L}]}{|Q_{\nu\mathbf{q}}^{\alpha L}|^2 (z_{\nu\mathbf{q}}^2 + 1)}, \quad (3)$$

with

$$z_{\nu\mathbf{q}} \equiv \frac{\hbar\omega - \hbar\omega_{\nu\mathbf{q}}}{\Gamma_{\nu\mathbf{q}}}, \quad (4)$$

where N is the number of unit cells in the sample, n_{imp} is the number density of defects, a_0 is the Bohr unit of length, $-e$ the electronic charge, α and L are related to the spatial direction of the current operator (x or y) and the defect scattering site in the graphene unit cell (A or B). Also, ν is a phonon mode label and \mathbf{q} is a momentum restricted to the First Brillouin zone; thus $\omega_{\nu\mathbf{q}}$ is the frequency and $\Gamma_{\nu\mathbf{q}}$ is related to the lifetime of the phonon labelled by $(\nu\mathbf{q})$. The contribution to the conductivity of Eq. (3) is composed of a sum over the whole First Brillouin zone of Fano-like terms with unitless Fano parameters $Q_{\nu\mathbf{q}}^{\alpha L}$ and amplitudes $A_{\nu\mathbf{q}}^{\alpha L}$. These parameters are related to the “Loop” function $\mathcal{H}_{\nu\mathbf{q}}^{\alpha L}$, corresponding to the sub-diagram of Fig. 2(d), which can be expressed as the sum of a “reactive” and “absorptive” term,

$$\mathcal{H}_{\nu\mathbf{q}}^{\alpha L} = \mathcal{R}_{\nu\mathbf{q}}^{\alpha L} + i\mathcal{I}_{\nu\mathbf{q}}^{\alpha L}, \quad (5)$$

such that, in atomic units,

$$Q_{\nu\mathbf{q}}^{\alpha L} \equiv -\frac{\mathcal{R}_{\nu\mathbf{q}}^{\alpha L}}{\mathcal{I}_{\nu\mathbf{q}}^{\alpha L}} \quad \text{and} \quad A_{\nu\mathbf{q}}^{\alpha L} \equiv \frac{1}{\hbar\omega_{\nu\mathbf{q}}} \frac{1}{4\Gamma_{\nu\mathbf{q}}} \left| \mathcal{R}_{\nu\mathbf{q}}^{\alpha L} \right|^2. \quad (6)$$

Given the asymmetrical nature of the spectrum, it will be useful below to define the phonon coupling strength [22],

$$P_{\nu\mathbf{q}} \equiv \frac{1}{4} \sum_{\alpha=x,y} \sum_{L=A,B} \frac{1}{\hbar\omega_{\nu\mathbf{q}}} \left(\left| \mathcal{R}_{\nu\mathbf{q}}^{\alpha L} \right|^2 + \left| \mathcal{I}_{\nu\mathbf{q}}^{\alpha L} \right|^2 \right), \quad (7)$$

as a measure of the weight of the mode.

It is useful at this point to draw parallels between the proposed contribution to the current-current correlation function and the theory of Raman scattering with a single phonon emission, presented diagrammatically in Fig. 2(c), along with the Loop function in Fig. 2(d). As depicted schematically in Fig. 2(e), the Loop function may be described as the absorption of a photon to a virtual excited state, followed by an elastic collision with a defect back to the electronic band of graphene. If the whole scattering process is in resonance both in momentum and energy with an optical phonon mode, then the cycle is similar to a Raman resonant transition, as also represented on Fig. 2(e), but with two major differences: on the one hand, elastic scattering with defects allow for intra- and intervalley processes within the Loop function; large \mathbf{q} phonon modes thus become available through this scheme. Also, in Raman spectroscopy the incoming light is energetic enough to induce interband transitions, whereas infrared light cannot: thus the resonant transition in the Loop function imposes that both momenta \mathbf{k} and $\mathbf{k} + \mathbf{q}$ be within $\hbar\omega$ of the Fermi energy, where $\hbar\omega$ is the energy of the incoming infrared light. There is always

a \mathbf{k} satisfying the resonant condition for

$$\frac{\omega}{v_F} \leq |\mathbf{q} - \mathbf{P}| \leq 2k_\mu + \frac{\omega}{v_F} \quad (8)$$

where k_μ is the radius of the circular Fermi surface and v_F is the Fermi velocity of graphene. In the above, $\mathbf{P} = \Gamma$ for intravalley \mathbf{q} and $\mathbf{P} = \pm \mathbf{K}$ for intervalley \mathbf{q} . If \mathbf{q} is such that Eq. (8) cannot be satisfied, we expect nonresonant (and thus small) contributions to the current-current correlation function.

Simulation of optical conductivity

To test the quantitative validity of the model, the contribution of Eq. (3) was computed within the tight-binding approximation in the spirit of the work of Peres *et al.* [24]. Impurity scattering is modeled in terms of on-site, randomly located impenetrable potentials, treated in a way to make use of the Full Born Approximation [24]. The phonon frequencies and polarization vectors were obtained from a force constant model [25]; the phonon dispersion was modified in the vicinity of $\pm \mathbf{K}$ to account for the physically well established Kohn anomalies at these points [26], but which the force constant model fails to capture. The parameters entering the electron-phonon coupling matrix elements were obtained by comparing with computed results available in the literature at $\mathbf{q} = \Gamma$ and $\mathbf{q} = \mathbf{K}$ [26, 27] (see Supplementary Information). The model contributions were computed for various chemical potential values μ at a graft density of 2%, a phonon energy broadening $\Gamma_{\nu\mathbf{q}} = 2.5$ meV, and an electronic energy broadening $\Gamma = 75$ meV (as exposed in Sec. III-B of the Supplementary Information, we estimate $\mu \simeq -450$ meV).

The model conductivity of Eq. (3) is compared to the experimental conductivity in the presence of disorder and soaked in a 1 mM DDQ solution in Fig. 3. The model reproduces the position and asymmetry of the two prominent bands in the baseline-corrected signal, and yields a roughly correct amplitude, given the uncertainty on the experimental chemical potential and Drude peak width. Also, it correctly captures the *transmission windows* signal profile (*i.e.* downward bands in the optical conductivity, upward bands on a transmittance scale) due to an interference effect between electron and phonon degrees of freedom, akin to the one captured by the intuitive extension of the Drude model. Finally, the contribution of the model to the conductivity vanishes as $\mu \rightarrow 0$, in agreement with the experimental observation that the asymmetric bands disappear upon soaking in hydrazine solution. For completeness, the conductivity was also computed for various reasonable values of the broadening parameter Γ : the asymmetry of the bands follows the same trend as that of the simple Drude-like model of Eq. (1) even when disorder is treated beyond lifetime

effects (See Fig. S10 and S11(b) of the Supplementary Information).

Fig. 3(b) shows that the phonon coupling strength (red areas) is substantial only near regions where the resonance conditions are satisfied (grey bands). This behavior leads to a coupling strength density of states with two major peaks corresponding to contributions coming from $\mathbf{q} \simeq \pm \mathbf{K}$ and $\mathbf{q} \simeq \Gamma$, as plotted in Fig. 3(a) (top panel, right axis).

DISCUSSION

The two prominent antiresonances in the experimental data can now readily be explained. The feature at $\sim 1600 \text{ cm}^{-1}$ comes from coupling to phonons near the E_{2g} mode for $\mathbf{q} \sim \Gamma$; in agreement with experiments, the amplitude of the simulated band increases with $|\mu|$, while the position of the band remains unchanged, reflecting the lack of phonon dispersion near the E_{2g} mode at Γ . The broad feature in the vicinity of $1200\text{--}1400 \text{ cm}^{-1}$ comes from coupling to phonons near the A'_1 mode for $\mathbf{q} \sim \pm \mathbf{K}$; again, the simulated amplitude of the band increases with $|\mu|$ as observed experimentally, and its position moves to higher energy with $|\mu|$ [dashed line in Fig. 3(a) tracking the position of the minimum], a consequence of the strong phonon dispersion near the Kohn anomaly at $\pm \mathbf{K}$. We note the absence of features around $\sim 1050 \text{ cm}^{-1}$, the frequency of the A'_2 mode at $\pm \mathbf{K}$: this absence is consistent with simulations based on density functional theory suggesting that the electron-phonon coupling strength of this mode is negligible [28].

Our experiments bring to light a disorder and phonon mediated phenomenon in single layer graphene yielding transmission windows at phonon frequencies matching $\mathbf{q} \sim \Gamma$ and $\mathbf{q} \sim \pm \mathbf{K}$. Unlike the contribution leading to Fano resonances in pristine multilayer graphene, the proposed mechanism is *intragrand* in nature and accounts for disorder beyond lifetime effects: electrons in states near the Fermi energy scatter coherently on defects and phonons, thus breaking the optical selection rule (*i.e.* $\mathbf{q} \simeq \Gamma$) valid in pristine samples. Whereas Fano profiles are induced by a *discrete state-continuum* coupling between Γ phonon modes and electronic degrees of freedom, the mechanism presented here involves *continuum-continuum* coupling, with phonon momenta constrained to small regions near Γ and $\pm \mathbf{K}$.

This phenomenon may prove useful in quantifying the disorder in graphene, and it will allow the modulation of the optical conductivity in a narrow terahertz band, hence providing extended tools for telecommunications, medical and security imaging, and novel analytic and sensing capabilities. Our model for single layer graphene is also expected to hold in other systems: in particular, the infrared spectroscopy of bilayer [8, 9] and few-layer [23] graphene, as well as carbon nanotubes [12],

should be revisited, as there too shall disorder enable phonon-mediated intra- and intervalley scattering.

* Michel.Cote@umontreal.ca

† r.martel@umontreal.ca

- [1] Low, T. & Avouris, P. Graphene Plasmonics for Terahertz to Mid-Infrared Applications. *ACS Nano* **8**, 1086–1101 (2014).
- [2] Horng, J. *et al.* Drude conductivity of Dirac fermions in graphene. *Physical Review B* **83**, 165113 (2011).
- [3] Zallen, R. Symmetry and Reststrahlen in Elemental Crystals. *Physical Review* **173**, 824–832 (1968).
- [4] Ju, L. *et al.* Graphene plasmonics for tunable terahertz metamaterials. *Nature Nanotechnology* **6**, 630–634 (2011).
- [5] Yan, H. *et al.* Damping pathways of mid-infrared plasmons in graphene nanostructures. *Nature Photonics* **7**, 394–399 (2013).
- [6] Brar, V. W. *et al.* Electronic modulation of infrared emissivity in graphene plasmonic resonators. *Nature Communications* **6**, 7032 (2015).
- [7] Yan, H. *et al.* Tunable infrared plasmonic devices using graphene/insulator stacks. *Nature Nanotechnology* **7**, 330–334 (2012).
- [8] Kuzmenko, A. *et al.* Gate Tunable Infrared Phonon Anomalies in Bilayer Graphene. *Physical Review Letters* **103**, 116804 (2009).
- [9] Tang, T.-T. *et al.* A tunable phonon-exciton Fano system in bilayer graphene. *Nature Nanotechnology* **5**, 32–36 (2010).
- [10] Yan, H., Low, T., Guinea, F., Xia, F. & Avouris, P. Tunable phonon-induced transparency in bilayer graphene nanoribbons. *Nano Letters* **14**, 4581–4586 (2014).
- [11] Thomsen, C. & Reich, S. Double Resonant Raman Scattering in Graphite. *Physical Review Letters* **85**, 5214–5217 (2000).
- [12] Lapointe, F. *et al.* Fano Resonances in the Midinfrared Spectra of Single-Walled Carbon Nanotubes. *Physical Review Letters* **109**, 097402 (2012).
- [13] Han, Z. *et al.* Homogeneous Optical and Electronic Properties of Graphene Due to the Suppression of Multilayer Patches During CVD on Copper Foils. *Advanced Functional Materials* **24**, 964–970 (2014).
- [14] Suk, J. W. *et al.* Transfer of CVD-grown monolayer graphene onto arbitrary substrates. *ACS Nano* **5**, 6916–6924 (2011).
- [15] Baranton, S. & Bélanger, D. Electrochemical derivatization of carbon surface by reduction of in situ generated diazonium cations. *The Journal of Physical Chemistry. B* **109**, 24401–24410 (2005).
- [16] Gan, L., Zhang, D. & Guo, X. Electrochemistry: an efficient way to chemically modify individual monolayers of graphene. *Small (Weinheim an der Bergstrasse, Germany)* **8**, 1326–1330 (2012).
- [17] Wang, Q. H. *et al.* Understanding and controlling the substrate effect on graphene electron-transfer chemistry via reactivity imprint lithography. *Nature Chemistry* **4**, 724–732 (2012).
- [18] Niyogi, S. *et al.* Covalent Chemistry for Graphene Electronics. *The Journal of Physical Chemistry Letters* **2**,

- 2487–2498 (2011).
- [19] Reich, S. & Thomsen, C. Raman spectroscopy of graphite. *Philosophical transactions. Series A, Mathematical, physical, and engineering sciences* **362**, 2271–2288 (2004).
 - [20] Mahan, G. *Many-Particle Physics* (Kluwer Academic, 2000).
 - [21] Cappelluti, E., Benfatto, L. & Kuzmenko, A. Phonon switching and combined Fano-Rice effect in optical spectra of bilayer graphene. *Physical Review B* **82**, 041402(R) (2010).
 - [22] Cappelluti, E., Benfatto, L., Manzardo, M. & Kuzmenko, A. B. Charged-phonon theory and Fano effect in the optical spectroscopy of bilayer graphene. *Physical Review B* **86**, 115439 (2012).
 - [23] Li, Z. *et al.* Structure-Dependent Fano Resonances in the Infrared Spectra of Phonons in Few-Layer Graphene. *Physical Review Letters* **108**, 156801 (2012).
 - [24] Peres, N. M. R., Guinea, F. & Castro Neto, A. H. Electronic properties of disordered two-dimensional carbon. *Physical Review B* **73**, 125411 (2006).
 - [25] Dubay, O. & Kresse, G. Accurate density functional calculations for the phonon dispersion relations of graphite layer and carbon nanotubes. *Physical Review B* **67**, 035401 (2003).
 - [26] Lazzeri, M., Attaccalite, C., Wirtz, L. & Mauri, F. Impact of the electron-electron correlation on phonon dispersion: Failure of LDA and GGA DFT functionals in graphene and graphite. *Physical Review B* **78**, 081406 (2008).
 - [27] Jiang, J. *et al.* Electron-phonon matrix elements in single-wall carbon nanotubes. *Physical Review B* **72**, 235408 (2005).
 - [28] Piscanec, S., Lazzeri, M., Mauri, F., Ferrari, A. & Robertson, J. Kohn Anomalies and Electron-Phonon Interactions in Graphite. *Physical Review Letters* **93**, 185503 (2004).

ACKNOWLEDGEMENTS

The authors acknowledge insightful discussions with Didier Mayou and Gabriel Antonius, as well as technical assistance from Pierre Lévesque.

Research described in this paper was partly performed at the Mid-IR beamline of the Canadian Light Source, which is supported by the Natural Sciences and Engineering Research Council of Canada, the National Research Council Canada, the Canadian Institutes of Health Research, the Province of Saskatchewan, Western Economic Diversification Canada, and the University of Saskatchewan. The authors thankfully acknowledge funding from the Natural Sciences and Engineering Research Council of Canada (NSERC) and le Fond de Recherche du Québec - Nature et Technologies (FQRNT). Simulations were performed on the infrastructures of Calcul Québec.

AUTHORS CONTRIBUTIONS

B.R. and F.L. contributed equally to this article. B.R. and M.C. devised the models and performed the simulations. F.L., E.G. and R.M. designed the experiments. Acquisition of the IR spectra was done by F.L., M.N., M.B. and R.M. F.L. and M.N. functionalized graphene. F.L., M.N., M.B., E.G. and S.C. proceeded to sample preparation and characterization of the graphene layers. Z.H. and V.B. provided the single layer graphene samples. B.R., F.L., M.C. and R.M. wrote the manuscript. All authors contributed to discussion and revision of the article.

COMPETING FINANCIAL INTERESTS

The authors declare no competing financial interests.